PCCP

PAPER

View Article Online
View Journal | View Issue

Cite this: *Phys. Chem. Chem. Phys.*, 2026, **28**, 5981

The accuracy of carbon-13 NMR magnetic-shielding tensors calculated using periodic DFT: a case study on the distinction of crystalline serine phases

Kathrin Rübartsch,[a] Leeroy Hendrickx,[ab] Ettore Bartalucci,[ab] Maksim Plekhanov,[c] Mirijam Zobel,[c] Carsten Bolm,[d] Maria Fyta *[ef] and Thomas Wiegand *[ab]

Received 2nd December 2025,
Accepted 31st January 2026

DOI: 10.1039/d5cp04690d

rsc.li/pccp

Carbon-13 nuclear magnetic resonance (NMR) spectroscopic fingerprints enable the unambiguous identification of a chemical compound. *Ab initio* calculations of NMR magnetic-shielding tensors are crucial for facilitating spectral resonance assignment, but require an accuracy on the order of one ppm or even less for carbon-13 for distinguishing structurally rather similar compounds, such as structural isomers and polymorphs. Using quantum-mechanical calculations within the density functional theory (DFT) approach and solid-state NMR spectroscopy under magic-angle spinning (MAS) conditions, we herein explore whether the accuracy of current DFT levels is sufficient to distinguish between three distinct solid phases of the amino acid serine using computer simulations. In that vein, enantiopure L-serine, L-serine monohydrate, and racemic DL-serine have been studied. Using solid-state calculations employing periodic boundary conditions, we computed NMR observables, such as ^{13}C isotropic magnetic-shielding values and ^{13}C magnetic-shielding anisotropy parameters of these phases. Different levels of DFT theory utilizing distinct exchange correlation functionals were tested in optimizing the hydrogen-atom positions prior to NMR observable calculations, which significantly improved the agreement with the experimental values. The comparison of the measured and the calculated observables confirmed the distinction between the serine phases not only experimentally but also by DFT calculations. We also compare the DFT-calculated NMR observables with predictions from a recently proposed machine learning (ML) approach. Our analysis clearly revealed that a rather low-cost exchange correlation functional in periodic solid-state DFT calculations reaches the desired accuracy of ^{13}C magnetic-shielding tensor calculations, provided that highly accurate initial structures are applied. These results underline that complementary experimental and computational studies can provide key insights into molecular systems and the interactions therein, enabling the distinction of structurally similar compounds (often polymorphs), which is of particular importance in pharmaceutics.

Introduction

The unambiguous distinction of polymorphs (or sometimes even pseudo-polymorphs, where solvent molecules are embedded in the crystal structure) is of paramount importance, for instance, in the field of pharmaceutics.[1,2] NMR crystallography[3–11] enables the determination of the structures of such polymorphic species. Solid-state NMR spectroscopy under magic-angle spinning (MAS) conditions plays an important role in the NMR crystallography toolbox and generally serves as a valuable tool for spectroscopically distinguishing polymorphic species, as illustrated for various examples.[12–22] Typically, the isotropic magnetic-shielding value (or in the case of spectra that have been referenced to a standard compound, the chemical shift value), which is defined

---

[a] Institute of Technical and Macromolecular Chemistry, RWTH Aachen University, Worringerweg 2, 52074 Aachen, Germany
[b] Max Planck Institute for Chemical Energy Conversion, Stiftstr. 34-36, 45470 Mülheim/Ruhr, Germany. E-mail: thomas.wiegand@cec.mpg.de
[c] Institute of Crystallography, RWTH Aachen University, Jägerstraße 17-19, 52066 Aachen, Germany
[d] Institute of Organic Chemistry, RWTH Aachen University, Landoltweg 1, 52074 Aachen, Germany
[e] Computational Biotechnology, RWTH Aachen University, Worringerweg 3, 52074 Aachen, Germany. E-mail: mfyta@biotec.rwth-aachen.de
[f] Center for Computational Life Sciences (CCLS), RWTH Aachen University, Aachen, Germany

as the average value of the trace of the 3 × 3 magnetic-shielding tensor, is sufficient to allow the spectroscopic distinction of those, although the magnetic-shielding anisotropy provides additional information about the electronic structure of the nucleus-of-interest. The latter can, for instance, be reported in the Herzfeld–Berger convention,[23] in which the span (Ω) reports the strength of the anisotropy (the widths of the static powder NMR lineshape) and the skew (κ) is a measure of the asymmetry of the tensor.

The accuracy of *ab initio* calculations of NMR magnetic-shielding tensors is crucial for supporting spectral resonance assignment, particularly for distinguishing polymorphs, often with minor structural differences.[13,24] *Ab initio* calculations of NMR observables are typically performed in the DFT framework[25] using either Gaussian- or Slater-type orbitals.[26] In most molecular species, high-level gas phase calculations on monomers (or smaller molecular clusters) are often sufficient, since the NMR observables are mainly dominated by local properties. However, particularly in cases where intermolecular interactions are of importance, solid-state calculations using plane-wave basis sets need to be performed,[27–30] which involves significantly higher computational costs, often restricting the DFT calculations to a lower level-of-theory and limiting the accuracy of the results.[31] In such methods, the gauge-including projector-augmented wave (GIPAW) approach is used.[32–35] Alternatively, quantum mechanics/molecular mechanics calculations have also been reported to compute solid-state NMR observables for molecular solids.[31] In the past few years, machine learning models have also entered the field, enabling a rather efficient prediction of magnetic-shielding parameters.[36–38]

Some of us have recently studied three distinct phases of the amino acid serine in the context of mechanochemical molecular-recognition processes.[39] The enantiopure phase of serine (L- and D-serine, respectively, both giving identical ^{13}C solid-state NMR spectra[40]) shows a different ^{13}C spectroscopic fingerprint than the racemic phase (DL-serine) with average ^{13}C chemical-shift differences on the order of 2 ppm.[39] The third serine phase we have observed in the course of our studies was the monohydrate L-serine phase (L-serine·H_2O),[41] which has been subjected to detailed solid-state NMR investigations before.[42] The chemical-shift values (^{1}H and ^{13}C) of several amino acids[43] have been calculated using GIPAW DFT with the PBE functional in previous work.[44,45] These values were further corrected using the isolated-molecule correction scheme, in which the differences in isotropic magnetic-shielding values at a PBE and PBE0 level-of-theory for a single molecule are calculated.[38,46] A mean absolute error of around 1.5 ppm was determined for ^{13}C isotropic magnetic-shielding values.[43] Recently, a very detailed study employed the experimentally determined ^{13}C isotropic chemical-shielding values of 20 solid amino acids (the L-enantiomers have been studied) for benchmarking periodic GIPAW calculations with GGA, meta-GGA, and hybrid DFT functionals.[20] Interestingly, best agreement between the experimental and calculated values has been achieved for the GGA level-of-theory (PBE functional).[20]

We herein study whether the current accuracy of plane-wave DFT calculations is sufficient to unambiguously distinguish the three serine phases mentioned above using ^{13}C magnetic-shielding tensor calculations. Based on initial benchmarks on the main DFT parameters and detailed test calculations for the different structures and exchange correlation functionals, we propose a strategy for periodic DFT calculations of interacting molecular systems. We do not intend to benchmark, as recently described in an excellent article,[20] but aim at illustrating, for our specific example, the potential of plane-wave periodic DFT calculations in calculating ^{13}C magnetic-shielding tensors, enabling the distinction of polymorphs. Our studies particularly highlight the importance of an accurate starting structure for such calculations (as often provided by single-crystal X-ray or neutron diffraction),[47] which indeed allows the distinction between the separate serine phases, thus reproducing experimentally observed trends.

Experimental

All chemicals employed in this work were obtained from commercial sources (see Table 1). The materials (except for DL-serine used for the experiments at 16.4 T) were ball milled for 20 min at 25 Hz in a 10 mL stainless-steel jar with one 10 mm stainless steel milling ball. The ball mill used was a MM400 shaker ball mill (RETSCH, Haan, Germany). DL-Serine measured at a magnetic-field strength of 16.4 T was milled for 20 min at 25 Hz in a 10 mL stainless-steel multi-cavity jar with three 7 mm stainless-steel milling balls. The ball mill used was a mixer mill MM500 nano (RETSCH, Haan, Germany). The L-serine monohydrate samples were prepared by mixing 50 mg of L-serine with 15 µL of de-ionized water in a 2 mL snap cap vial followed by processing in the resonant acoustic mixer LabRAM I (Resodyn Acoustic Mixers, Butte, Montana, USA) for 20 min at 100 g.

Solid-state NMR experiments

Solid-state NMR experiments were performed in 3.2 mm zirconia rotors with Vespel caps (Bruker BioSpin) in a 3.2 mm standard Bruker triple-resonance HXY probe on a 500 MHz Bruker NMR-spectrometer (AVANCE III HD console) as well as in a 3.2 mm standard Bruker double-resonance HX probe on a 700 MHz Bruker NMR-spectrometer (AVANCE NEO console). For each slow-spinning ^{1}H–^{13}C CP-MAS spectrum recorded with an MAS frequency of 2.0 kHz, a lineshape simulation using the software ssNake (version 1.5)[48] was performed to determine the chemical-shift anisotropy parameters. All details of the performed experiments are given in Tables S1 and S2, SI.

Table 1 Reference list of used chemicals, their CAS number and the commercial distributor

	CAS number	Purity	Manufacturer
L-Serine	56-45-1	99%	abcr GmbH (Karlsruhe, Germany)
DL-Serine	302-84-1	99%	abcr GmbH (Karlsruhe, Germany)
Water	—	De-ionized	—

X-ray crystallography

The powder X-ray diffraction (PXRD) patterns were collected on a D8 Advance diffractometer (Bruker, Karlsruhe, Germany) operating in Bragg–Brentano geometry, using a flat circular sample holder with a sample thickness of 0.5 mm and a diameter of 10 mm. Cu-tube and a Ni-filter (Cu K_α radiation $\lambda = 1.5406$ Å) at a tube voltage of 40 kV together with a LYNXEYE semiconductor strip detector were used. Measurements were carried out at room temperature over a 2θ range of 10–60° (corresponding to a momentum transfer Q range of 0.71–4.1 $Å^{-1}$), with a step size of 0.0105° and a counting time of 3 s per step. Structure refinements were performed using GSAS-II software (version 5609).[49]

Computational details

DFT calculations were performed as implemented in the Vienna *ab initio* Simulation Package (VASP) (version 6.4.3).[50–53] For the geometry optimizations using the conjugate gradient algorithm, an energy cutoff of 1×10^{-6} eV, Gaussian smearing with a width of 0.01 eV, and a regular $3 \times 3 \times 3$ k-point mesh for integration in the Brillouin zone were chosen as convergence criteria after careful benchmarks, as can be seen in Fig. S1–S3.[54] The Kohn–Sham orbitals were expanded in a plane-wave basis set with a kinetic energy cutoff of 500 eV. Different approaches for the exchange–correlation effects were applied, including the GGA PBE, meta-GGA TPSS, or hybrid functionals HSE06 and B3LYP.[44,45,55–57] The DFT-D3 dispersion correction with the zero-damping function was used.[58] Magnetic-shielding tensors were computed using the GIPAW method and PBE-functional. The isotropic chemical-shift values δ reported using VASP for nucleus in the molecule-of-interest correspond to the negative of the calculated magnetic-shielding values σ ($\delta_{\text{iso}}^{\text{calc,VASP}} \approx -\sigma_{\text{iso}}^{\text{calc,VASP}} + \sigma_{\text{iso,ref}}^{\text{calc,VASP}}$, with $\sigma_{\text{iso,ref}}^{\text{calc,VASP}}$ representing the calculated isotropic magnetic-shielding value of the considered nucleus in a reference molecule, which was not further considered in this work).[32,44,45,59] The "G = 0 including" chemical-shift values that consideronly the valence contribution are reported, with $G = 0$ taking the induced magnetic-field caused by the macroscopic magnetic-susceptibility tensor into account.[60] Standard plane augmented wave (PAW) pseudopotentials were used for all atomic species.[61]

The crystal structures of serine considered in this work were taken from the Cambridge Structural Database (CSD), with access codes LSERIN18, LSERMH10, and DLSERN11.[62,63] Table 2 provides an overview of the corresponding CSD IDs and original publications, showing which structure was used to represent the crystalline phases L-serine, L-serine monohydrate, and DL-serine, respectively.

Table 2 Overview of CSD IDs used herein for L-serine, L-serine·H_2O, and DL-serine

	CSD ID	Ref.
L-Serine	LSERIN18	56
L-Serine·H_2O	LSERMH10	57
DL-Serine	DLSERN11	57

If not reported otherwise, all three structures were geometrically optimized by allowing only the hydrogen atoms to move freely. For the calculation of NMR parameters, two distinct approaches were employed: (i) direct computation of magnetic-shielding tensors using the database structure without any relaxation with DFT and (ii) prior optimization of hydrogen-atom positions using various levels of theory, that is, various exchange correlation (XC) DFT functionals, while keeping the unit-cell parameters fixed. Specifically, we performed various calculations of the three structures and the different XC functionals without or with structural optimization. We refer to these as 'no opt.' or 'X' (X = functional), respectively. For comparison with the DFT calculations, we applied the machine learning (ML) model ShiftML3 to compute magnetic shielding tensors,[36] using either the structures as directly obtained from the CSD or geometries resulting from hydrogen-atom optimization at the B3LYP level-of-theory using VASP.

Results and discussion

Solid-state NMR characterization of three distinct serine phases

Upon studying mechanochemically induced molecular-recognition events, we came across the example of amino acids, for which ball milling or resonant acoustic mixing (RAM) of an equimolar ratio of the D- and L-amino acids provided the corresponding racemic phases (DL-amino acid), with the latter requiring liquid-assisted RAM conditions.[39,41] This has been illustrated for the two examples of alanine and serine.[39,41] Carbon-13 detected solid-state NMR spectroscopy has been used as the central analytical tool to distinguish such phases and to monitor the underlying solid-state molecular-recognition events.

Fig. 1 shows the ^1H–^{13}C cross-polarization (CP) spectra we have reported previously,[39,41] indeed showing that DL-serine and L-serine can be distinguished based on their characteristic spectral fingerprints. Chemical-shift differences of up to 3 ppm have been observed for the individual carbon atoms (for the isotropic ^{13}C chemical-shift values, see Table 3). We also prepared the L-serine monohydrate sample (in the following denoted as L-serine·H_2O) using a RAM device, whose C_α and C_β chemical-shift values resemble those of DL-serine. The carboxylic acid group carbon atoms, though, allow an unambiguous distinction of the three phases. Herein, we also explore the accuracy of plane-wave periodic DFT calculations in distinguishing such phases in computer simulations, requiring accuracies in the calculated ^{13}C isotropic chemical-shift values of around 1–2 ppm.

A central goal of this work is to compare the anisotropy of the magnetic-shielding tensor between experiment and DFT calculations. The anisotropy reveals important information about the local chemical environment of the nucleus-of-interest,[64,65] can be linked directly to electronic structures,[66,67] even enabling the understanding of chemical reactivities (for a recent review article, see ref. 68), and can reveal insights into molecular dynamics.[69] The magnetic-shielding interaction is described by a 3×3 tensor, which contains in the laboratory frame (LAB, in which the external magnetic field, B_0, points along the z-axis) nine independent components (see eqn (1)). By using rotation matrices involving the Euler angles α, β, and γ, this matrix can be diagonalized in a molecule-fixed frame

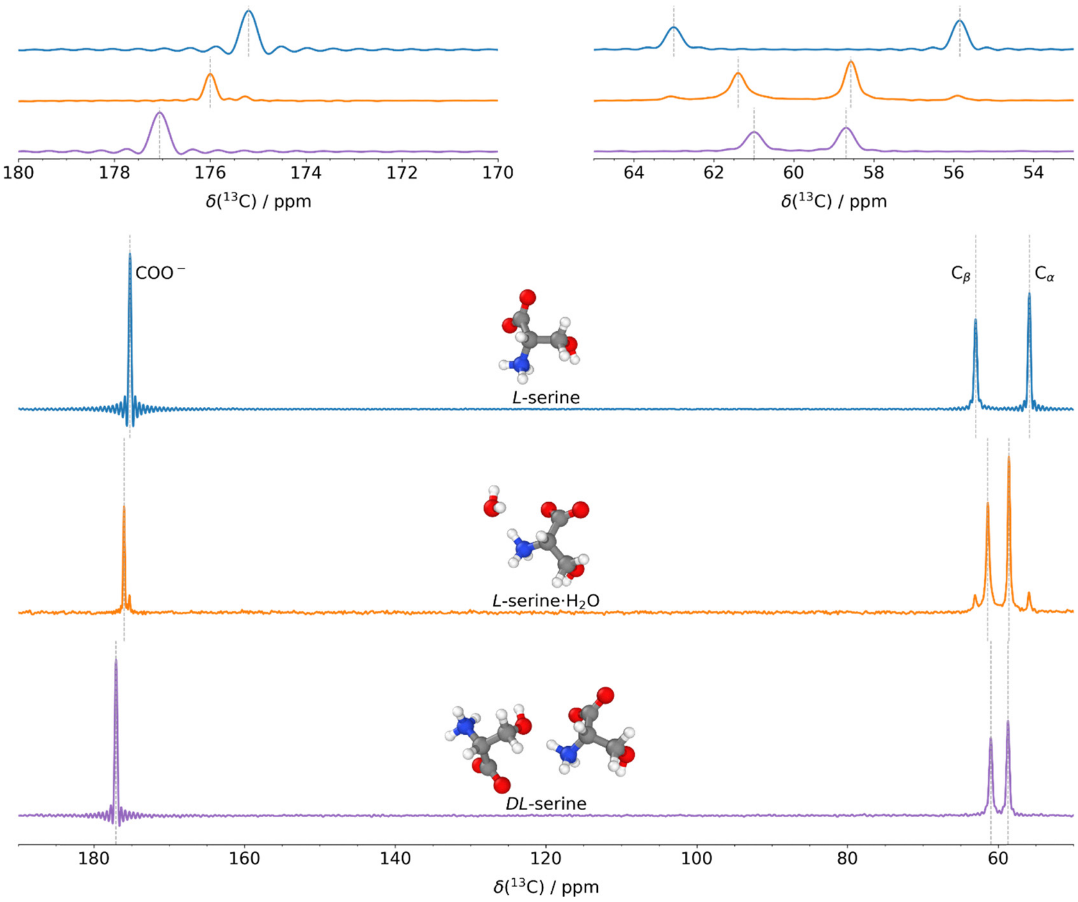

Fig. 1 ^{1}H–^{13}C CP-MAS NMR spectra of DL-serine (purple, bottom), L-serine·H$_2$O (orange, middle) and L-serine (blue, top) revealing distinct differences in the isotropic ^{13}C chemical-shift values of the phases. All spectra have been recorded at a magnetic-field strength of 11.7 T and a MAS frequency of 17.0 kHz. L-Serine·H$_2$O contains a small amount of L-serine. The spectra have already been published in our previous work, see ref. 39 and 41. The truncation visible in some of the spectra is caused by too short data acquisition times caused by probe limitations during high power ^{1}H decoupling. In addition, representative structures of the different serine phases based on the single-crystal structures (CSD codes DLSERN11, LSERMH10 and LSERIN18 for DL-serine, L-serine·H$_2$O and L-serine, respectively) are given. In the molecular stuctures hydrogen, carbon, oxygen, and nitrogen atoms are depicted in white, grey, red, and blue, respectively.

Table 3 Summary of isotropic ^{13}C chemical-shift values as determined from the experimental spectra shown in Fig. 1

	$\delta_{\text{iso}}^{\text{exp.}}$ (COO$^-$)/ppm	$\delta_{\text{iso}}^{\text{exp.}}$ (C$_\alpha$)/ppm	$\delta_{\text{iso}}^{\text{exp.}}$ (C$_\beta$)/ppm
L-Serine	175.2	55.9	63.0
L-Serine·H$_2$O	176.0	58.6	61.4
DL-Serine	177.1	58.7	61.0

(the principal axis system, PAS) and three independent components remain:

$$\underline{\sigma}^{(k,\text{LAB})} = \begin{pmatrix} \sigma_{xx}^{(k,\text{LAB})} & \sigma_{xy}^{(k,\text{LAB})} & \sigma_{xz}^{(k,\text{LAB})} \\ \sigma_{yx}^{(k,\text{LAB})} & \sigma_{yy}^{(k,\text{LAB})} & \sigma_{yz}^{(k,\text{LAB})} \\ \sigma_{zx}^{(k,\text{LAB})} & \sigma_{zy}^{(k,\text{LAB})} & \sigma_{zz}^{(k,\text{LAB})} \end{pmatrix} = R(\alpha,\beta,\gamma)\begin{pmatrix} \sigma_{xx}^{(k,\text{PAS})} & 0 & 0 \\ 0 & \sigma_{yy}^{(k,\text{PAS})} & 0 \\ 0 & 0 & \sigma_{zz}^{(k,\text{PAS})} \end{pmatrix} R^{-1}(\alpha,\beta,\gamma) \quad (1)$$

where $\sigma_{ij}^{(k,\text{LAB/PAS})}$ denotes the tensor components along the directions i,j in either the LAB or PAS coordinate systems and R is the Euler rotation matrix.

In solution, due to the fast Brownian motion, only the isotropic chemical-shift value (note that the chemical shift is obtained from the magnetic shielding by referencing to a standard compound) can be measured (which is 1/3 of the trace of the above reported tensor). In contrast to this, solid-state NMR allows the determination of all three principal-axis system components, for instance, by recording slow-spinning MAS spectra and simulating their lineshapes to envelopes of the static powder spectra[70] or by recording multidimensional isotropic-anisotropic correlation experiments.[71–74] In that vein, according to eqn (1), we determined the ^{13}C chemical-shift anisotropy (CSA) by recording slow-spinning MAS experiments (employing an MAS frequency of 2.0 kHz) at two different magnetic-field strengths (for the spectra at 11.7 T, see Fig. 2, and the spectra at 16.4 T are provided in Fig. S4). Lineshape simulations allow the determination of the span (Ω) and skew (κ) parameters (using the Herzfeld–Berger convention[23]). The respective results are summarized in Table 4, reporting only the

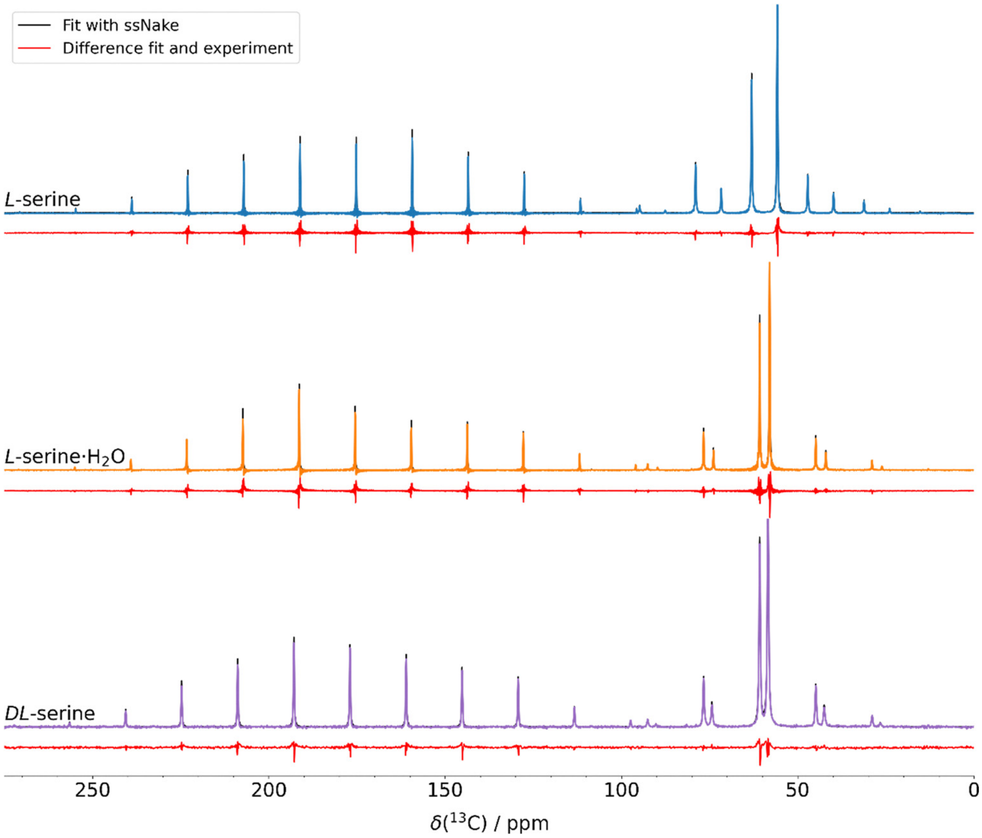

Fig. 2 Slow-spinning ^{1}H–^{13}C CP-MAS NMR spectra of DL-serine (purple, bottom), L-serine·H_2O (orange, middle) and L-serine (blue, top) recorded at a magnetic-field strength of 11.7 T and a MAS frequency of 2.0 kHz. Lineshape simulations are shown as black lines. Differences between the experiment and fit are shown in red as difference spectra.

Table 4 Overview of experimentally determined ^{13}C CSA parameters (11.7 T) for the carboxylic acid carbon of the three serine phases. In brackets, the values determined from the spectra recorded at 16.4 T are reported. n.d.: not determined

	$\Omega^{\text{exp.}}$ (COO^-)/ppm	$\kappa^{\text{exp.}}$ (COO^-)
L-Serine	130.8 [131.3]	−0.04 [−0.03]
L-Serine·H_2O	129.9 [n.d.]	0.2 [n.d.]
DL-Serine	135.8 [133.3]	0.09 [0.09]

values for the carboxylic group carbon, which exhibits the highest CSA. Rather similar Ω-values of around 130 ppm have been observed for the three different serine phases, whereas the κ-values range between −0.04 and 0.22. The results for C_α and C_β are displayed in Tables S3 and S4 of the SI, respectively.

We next attempted to establish a protocol for determining the agreement between the experimental data provided in Tables 3 and 4 and calculations of NMR magnetic-shielding tensors using DFT calculations under periodic-boundary conditions. As a matter of fact, finding a decent starting structure remains crucial for the calculations. We thus recorded the PXRD pattern of all three serine phases for which NMR spectra have been recorded. Crystal structures taken from the Cambridge Crystallographic database[75] were used for comparing the experimental and back-predicted patterns (Fig. 3). For L-serine, the structure LSERIN18[62] matches the diffraction pattern. For DL-serine, the best match has been observed for DLSERN11.[63] For L-serine·H_2O, a good agreement with the structure LSERMH10 has been found, taken into account its decomposition into L-serine over time.[63] All samples exhibit strong texture effects, resulting in changes in relative peak intensities. We concluded that the identified crystal structures revealed good agreement with the experimental PXRD pattern and decided to use those geometries in the complementary DFT calculations. The hydrogen-atom positions, however, were optimized in most cases prior to the NMR parameter calculations, as will be outlined further below. Note that while the structure of L-serine has been determined by X-ray diffraction, the structures of DL-serine and L-serine·H_2O were determined by neutron diffraction, already allowing us to assume more accurate hydrogen-atom positions (*vide infra*).

DFT-assisted calculation of solid-state NMR observables

After ensuring the accuracy of the database structures, we used these in periodic DFT calculations in order to extract the NMR observables. A comparison of the isotropic ^{13}C chemical-shift values and the CSA parameters for the carboxylic acid group (COO^-) is provided in Fig. 4 for the different DFT exchange correlation functionals used for optimizing the hydrogen-atom positions prior to the calculation of NMR observables. Specifically, this figure provides the comparison between experimental and

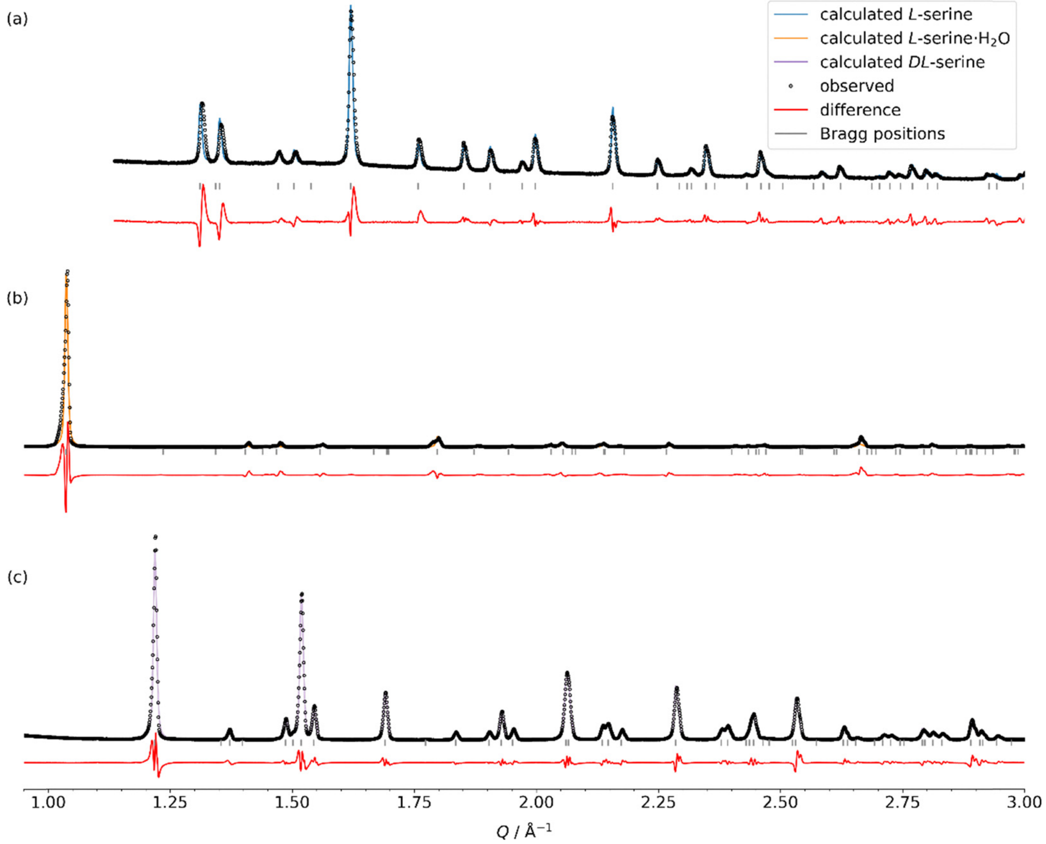

Fig. 3 Comparison of experimental PXRD patterns of the three serine phases (a) L-serine, (b) L-serine·H_2O and (c) DL-serine to the back-predicted ones using published single-crystal structures (see Table 2 for the corresponding CSD entries used).

calculated isotropic ^{13}C chemical-shift values for the difference in the chemical-shift values between the carboxyl acid group carbon and C_α (Fig. 4a), between the carboxyl acid group carbon and C_β (Fig. 4b) and between C_β and C_α (Fig. 4c) for the three different serine phases introduced above. These differences serve as a measure for the deviation between the experiment and plane-wave DFT calculations using various level-of-theories for the optimization of the hydrogen-atom positions prior to the magnetic-shielding tensor calculations. The data reveal that based on the calculations without structural relaxation, each crystal structure exhibited an overall distinct deviation from the experimental chemical-shift differences of up to 4.7 ppm for L-serine (LSERIN18), with DL-serine (DLSERN11) demonstrating the best match for the three isotropic chemical-shift differences (0.2 ppm for $COO^-–C_\alpha$, −1.2 ppm for $COO^-–C_\beta$ and 1.4 ppm for $C_\beta–C_\alpha$).

In general, the calculated chemical-shift difference between COO^- and C_α was found to be in better agreement with the experimental data than the corresponding difference between COO^- and C_β and between C_β and C_α. For calculations involving the relaxation of the hydrogen-atom positions only, the deviation between calculated and experimental chemical-shift differences varied depending on the level-of-theory used during the optimization. Except for DL-serine, the best agreement with experiment was achieved for hybrid functionals, such as B3LYP. The minimal deviations between computation and the experiment for the $C_\beta–C_\alpha$ chemical-shift difference have been determined to 2.6 ppm for L-serine (B3LYP), 1.4 ppm for L-serine·H_2O (B3LYP) and 1.2 ppm for DL-serine (HSE06). As noted above, smaller deviations ranging between 0.2 and −1.1 ppm for the minimal values are obtained for the $COO^-–C_\alpha$ difference. Larger deviations involving C_β chemical-shift values are attributed to higher uncertainties in their DFT-computed isotropic chemical-shift value, possibly as a consequence of intermolecular hydrogen-bond formation of the neighbored hydroxyl group. The overall better agreement for DL-serine and L-serine·H_2O compared to L-serine might point to the more accurate refinement of hydrogen-atom positions *via* neutron diffraction, leading to structures of higher quality than in the case of L-serine. These results highlight the crucial role of hydrogen-atom positioning in accurately predicting the isotropic ^{13}C chemical-shift differences, as already indicated in previous studies (for some examples, see ref. 28–30, 34, 35, and 76–78). For instance, ^{13}C magnetic-shielding tensor GIPAW calculations for α-glycine using different crystal structures revealed the best agreement with experimental values in most cases by only geometrically optimizing the hydrogen atom positions, instead of an all-atom optimization.[76] Whether a full geometry optimization even improves the agreement with experimental chemical-shift values further is under debate (as, for instance, such calculations would yield the geometry only at 0 K) and should be decided on a case-to-case basis as proposed

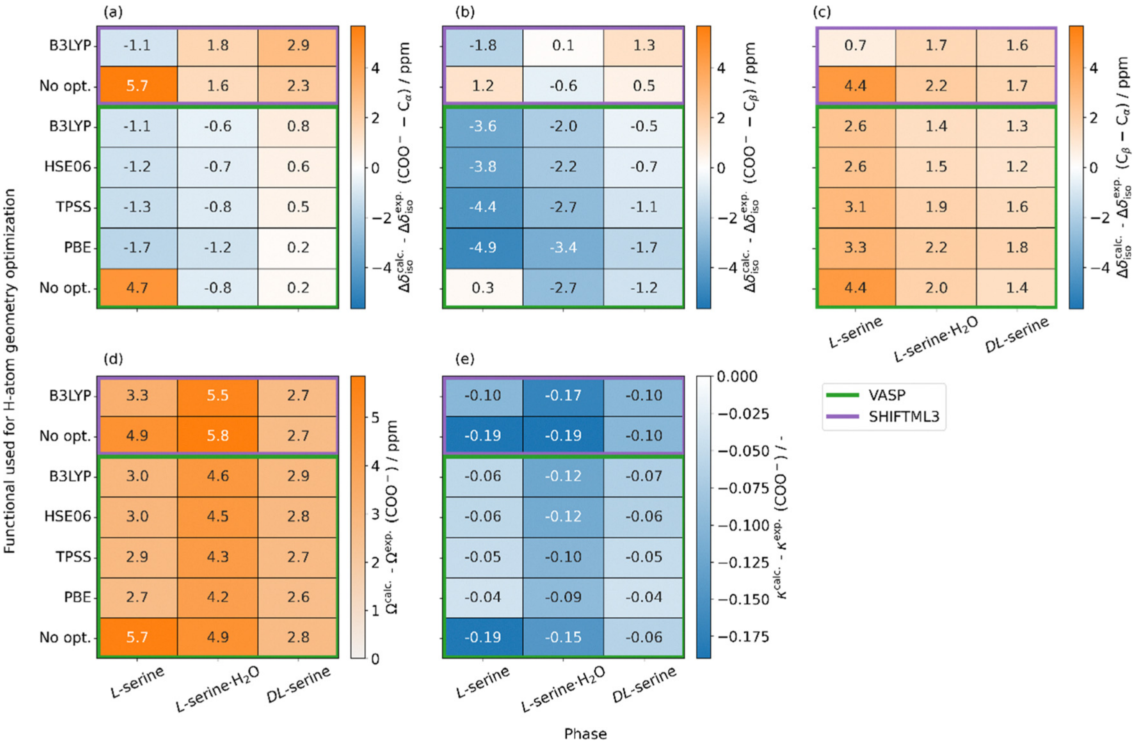

Fig. 4 "Heat maps" comparing experimental and DFT-calculated isotropic ^{13}C chemical-shift values. The differences between experimental and DFT-calculated values for the difference in the chemical-shift values between the carboxyl acid group carbon and C_α (a), between the carboxyl acid group carbon and C_β (b) and between C_β and C_α (c) for the three different serine phases are plotted in units of ppm. "Heat maps" of the CSA parameters Ω (d) and κ (e) only for COO$^-$ as a function of the DFT functional. In all cases (except no opt.) the hydrogen-atom positions were geometrically optimized in VASP before the calculation of the ^{13}C magnetic-shielding tensors using different DFT functionals, as indicated in the figure. In VASP (highlighted by the green lines), calculations of ^{13}C magnetic-shielding tensors have been performed in all cases with the PBE DFT functional. As comparison and separated by the purple lines, the results obtained by using the machine learning model ShiftML3 are shown.[36]

in ref. 30. In the case of the serine phase studied herein, optimizing the hydrogen-atom positions seems to be sufficient,[77] as full geometry optimization even leads to larger deviations from experimental values (*vide infra*).

We have also compared our experimental values with those obtained by the ML model ShiftML3, in which a ML model was trained on a database including periodic DFT-calculated magnetic-shielding tensors achieved at the PBE level-of-theory.[36] Similar to the observations for the DFT calculations, the deviations to the experimental values decrease for the geometry-optimized structures (Fig. 4a, b and c), pointing again to the importance of an accurate structure. Interestingly, the DFT calculated and the ML predicted data in this Fig. 4 show a different relationship relative to the experimental data. Specifically, the DFT calculations match better the experimental measurements in the case of the COO$^-$–C_α differences, while the ML model better captures the COO$^-$–C_β differences. Both methods reveal a similar accuracy for the C_β–C_α differences. Taking the low computational cost of ShiftML3 into consideration, though, this algorithm already pinpoints the power of ML in predicting ^{13}C magnetic-shielding tensors and it will probably even further improve with the increase of the accuracy in DFT-calculations of magnetic-shielding tensors (and thus the training data sets).

We next turn to the anisotropy of the ^{13}C magnetic-shielding tensors of the three serine phases. As mentioned above, only the carboxylic acid carbon is analyzed as the span-value is largest in magnitude and thus determined with much higher precision experimentally. The comparison in Ω- (Fig. 4c) and κ-values (Fig. 4d) between calculation and experiment, again using different DFT-functionals for the geometry optimization of the hydrogen-atom positions, reveals in all cases an overestimation of the Ω-values with the largest deviations of 4.9 and 5.7 ppm for L-serine·H_2O and L-serine without initial constrained geometry optimization. While the deviations in Ω-values between calculation and experiment reduce significantly for L-serine upon optimizing the hydrogen atom positions (minimal deviation of 2.7 ppm, PBE), the values for L-serine·H_2O and DL-serine do not change significantly (minimal deviations of 4.2 and 2.6 ppm, respectively). A similar trend is observed for the κ-values with minimal deviations of −0.04 (PBE), −0.09 (PBE) and −0.04 (PBE) for L-serine, L-serine·H_2O and DL-serine, respectively. Interestingly, the PBE GGA-functional revealed the best agreement between simulation and experiment in all cases. ShiftML3, as in the case of the DFT, overestimates the Ω-values, whereas for the κ-values in all cases, larger deviations are obtained by such ML-approaches as compared to the DFT calculations. Note that a geometry optimization allowing all atoms in the molecules to relax (PBE level-of-theory) provides a poorer agreement with nearly all of the respective experimental NMR observables in

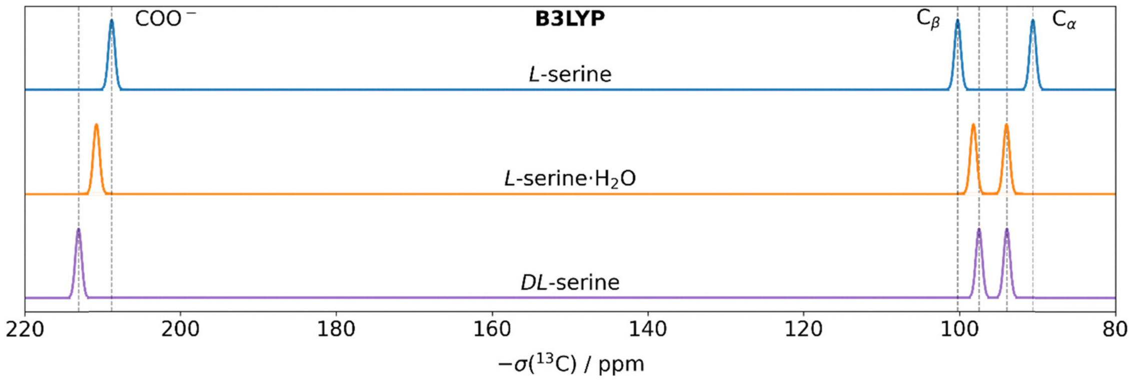

Fig. 5 Simulated ^{13}C NMR spectra of DL-serine (purple, bottom), L-serine·H_2O (orange, middle) and L-serine (blue, top) using the calculated isotropic ^{13}C magnetic-shielding values from VASP determined after optimizing the hydrogen atoms at a B3LYP level-of-theory. For visualisation, Gaussian functions were used with the calculated magnetic-shielding values as expected values and a standard deviation of 0.4 ppm. The dashed lines serve as guides to the eye.

Table 5 Summary of the differences in isotropic ^{13}C chemical-shift values computed using VASP as determined from the simulation of the calculated spectra shown in Fig. 5. The magnetic-shielding values were obtained after optimizing the hydrogen atoms at a B3LYP level-of-theory in VASP

	$\Delta\delta_{\text{iso}}^{\text{calc.}}$ (COO^-–C_α)/ppm	$\Delta\delta_{\text{iso}}^{\text{calc.}}$ (COO^-–C_β)/ppm	$\Delta\delta_{\text{iso}}^{\text{calc.}}$ (C_β–C_α)/ppm
L-Serine	118.2 (119.3[a])	108.6 (112.2[a])	9.7 (7.1[a])
L-Serine·H_2O	116.8 (117.4[a])	112.6 (114.6[a])	4.2 (2.8[a])
DL-Serine	119.2 (118.4[a])	115.6 (116.1[a])	3.6 (2.3[a])

[a] Experimental values.

our cases instead of optimizing the hydrogen atoms only (see Fig. S5, S8).

Fig. 5 shows schematically the ^{13}C NMR spectra for all three serine phases using the DFT-calculated isotropic magnetic-shielding values obtained after optimizing the hydrogen atoms at a B3LYP level-of-theory (for the further DFT functionals employed herein, see Fig. S6). When compared with the experimental spectra in Fig. 1, the computed ^{13}C chemical-shift values of the carboxylic acid group carbon atom reproduce the experimental order, with DL-serine having the highest chemical-shift value and L-serine the lowest. The same is observed for the C_β–C_α chemical-shift difference, with L-serine showing the largest value experimentally and DL-serine the smallest. Even the small deviations observed experimentally between L-serine·H_2O and DL-serine are qualitatively reproduced correctly. Although perfect reproduction of the experimental data is not possible (*i.e.* the differences in carboxyl group carbon chemical-shift values are overestimated; see Fig. 5), the three distinct serine phases can be qualitatively distinguished by means of DFT calculations. The same holds for the ShiftML3 predictions (Fig. S7). Note, though, that an optimization of the hydrogen atoms is required prior to the calculation of NMR observables, as discussed above (for the simulated spectra after full geometry optimization, see Fig. S8).

Computational time

As a final remark on the DFT computations of NMR observables, we assess the computational demand of these, especially with respect to their accuracy as observed in Table 5 and Fig. 6. To this end, we compare in Fig. 6 the total computational times needed for performing the respective NMR calculations as well

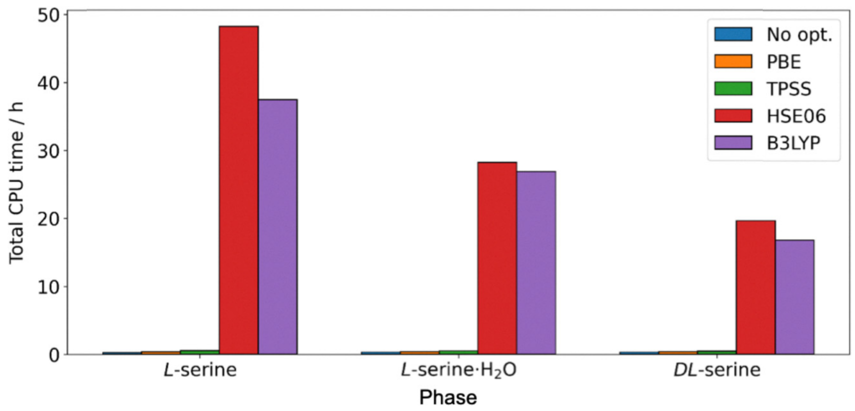

Fig. 6 Comparison of calculation times (using 36 CPU cores) for the three serine phases studied herein as a function of the DFT exchange correlation functional used for the optimization of the hydrogen atom positions.

as geometry optimizations of hydrogen-atom positions in VASP. We focus only on the relaxation part, as the computation of the NMR observables was performed at the same level corresponding computational times on the order of 20 min (using 36 CPU cores). Intuitively, the most complex and non-local HSE06 reflected an almost 50 time increase in time than the case without structural optimization for the semi-local PBE functional. A comparison of these trends to the accuracy shown in Fig. 6 clearly reveals that the longer computational times for the structural optimization do not compensate in the accuracy of the NMR observables. Accordingly, the assessment of all these results points to the use of less complex and computationally less demanding exchange correlation functionals for DFT for the calculations of the NMR observables, provided the use of accurate and high-quality initial structures. For the calculation of magnetic-shielding tensors using ShiftML3, executing the Python script for the six magnetic-shielding tensors reported herein required a computational time of only 26.6 s (using 36 CPU cores). ShiftML3 was found to be approximately 271 times faster than calculating NMR observables with DFT. The very low computational cost thus makes ShiftML3 well suited for fast initial benchmarks, but still needs to occasionally be enhanced by additional insights from the DFT-calculated observables.

Conclusions

Computer simulations within the DFT framework using periodic boundary conditions were compared against experimentally derived solid-state MAS NMR ^{13}C magnetic-shielding tensors for three serine phases, namely, L- and DL-serine, as well as L-serine·H_2O. Such phases can be distinguished experimentally based on ^{13}C isotropic chemical-shift differences, which are, however, small, on the order of only 2–3 ppm. Our test study of this challenging system reveals the importance of optimizing the hydrogen-atom positions prior to the calculations of the NMR parameters, which is key particularly for crystal structures derived from X-ray diffraction, in which the hydrogen-atom positions remain less well defined. Using this protocol, the experimental trends in isotropic ^{13}C magnetic-shielding values are reproduced correctly in the calculations, enabling an unambiguous distinction of the three phases. Similar conclusions hold for the anisotropy parameters, for which hydrogen-atom position optimization improves the agreement with experiment as well. Our work underlines that the use of a rather low-cost DFT exchange correlation functional for the constrained geometry optimizations already reveals decent agreement with experimental data, of similar magnitude to ShiftML3 predictions. For some observables, such as the COO^-–C_α differences and the skew κ, DFT still shows better agreement with the experiment than the ML model, with a higher computational load. Indeed, the use of more complex semi-local or non-local exchange correlation functionals for structural optimization slightly enhances the accuracy, but at the same time significantly increases the computational cost. Most importantly, the insights obtained from this comparative study and the thereby proposed calculation protocol provide the means for efficiently complementing experimental efforts in fingerprinting structural polymorphs and emphasize the applicability of periodic plane-wave DFT simulations.

Conflicts of interest

There are no conflicts to declare.

Data availability

Supplementary information is available. See DOI: https://doi.org/10.1039/d5cp04690d.

The scripts and data used in this manuscript will be made available through a public Radar4Chem repository hosted at DOI: https://doi.org/10.22000/7022jhfh8mwq5tyk.

Acknowledgements

This research was funded by the Deutsche Forschungsgemeinschaft (DFG, German Research Foundation) under Germany's Excellence Strategy – Exzellenzcluster 2186 ''The Fuel Science Center'' (ID: 390919832). T. W. acknowledges further support from the DFG (project number 455240421 and Heisenberg fellowship, project number 455238107) and the Max Planck Society. K. R. is grateful to Sabrina Smid and Longlong Li for assisting with technical issues of the simulations and Dr Ridvan Ince for assisting with the ssNake analysis. The computing time provided in the NHR Center NHR4CES at RWTH Aachen University (project number p0024945) is greatly acknowledged. This study was also funded by the Federal Ministry of Education and Research and the state governments participating on the basis of the resolutions of the GWK for national high-performance computing at universities. Open Access funding provided by the Max Planck Society.

References

1 E. H. Lee, *Asian J. Pharm. Sci.*, 2014, **9**, 163–175.
2 Q. Shi, H. Chen, Y. Wang, J. Xu, Z. Liu and C. Zhang, *Int. J. Pharm.*, 2022, **611**, 121320.
3 P. Hodgkinson, *Prog. Nucl. Magn. Reson. Spectrosc.*, 2020, **118–119**, 10–53.
4 R. K. Harris, R. E. Wasylishen and M. J. Duer, *NMR Crystallography*, Wiley, 2012.
5 B. Elena and L. Emsley, *J. Am. Chem. Soc.*, 2005, **127**, 9140–9146.
6 C. J. Pickard, E. Salager, G. Pintacuda, B. Elena and L. Emsley, *J. Am. Chem. Soc.*, 2007, **129**, 8932–8933.
7 F. Taulelle, *Solid State Sci.*, 2004, **6**, 1053–1057.
8 J. Senker, L. Seyfarth and J. Voll, *Solid State Sci.*, 2004, **6**, 1039–1052.

9 P. M. J. Szell, S. O. Nilsson Lill, H. Blade, S. P. Brown and L. P. Hughes, *Solid State Nucl. Magn. Reson.*, 2021, **116**, 101761.

10 L. Emsley, *Faraday Discuss.*, 2025, **255**, 9–45.

11 A. Hofstetter and L. Emsley, *J. Am. Chem. Soc.*, 2017, **139**, 2573–2576.

12 T. Wiegand, D. Ludeker, G. Brunklaus, K. Bussmann, G. Kehr, G. Erker and H. Eckert, *Dalton Trans.*, 2014, **43**, 12639–12647.

13 R. K. Harris, *Analyst*, 2006, **131**, 351–373.

14 J. Thun, L. Seyfarth, J. Senker, R. E. Dinnebier and J. Breu, *Angew. Chem., Int. Ed.*, 2007, **46**, 6729–6731.

15 M. R. Chierotti and R. Gobetto, *CrystEngComm*, 2013, **15**, 8599–8612.

16 A. Abraham, D. C. Apperley, T. Gelbrich, R. K. Harris and U. J. Griesser, *Can. J. Chem.*, 2011, **89**, 770–778.

17 H. Hamaed, J. M. Pawlowski, B. F. T. Cooper, R. Fu, S. H. Eichhorn and R. W. Schurko, *J. Am. Chem. Soc.*, 2008, **130**, 11056–11065.

18 S. A. Southern and D. L. Bryce, in *Annual Reports on NMR Spectroscopy*, ed. G. A. Webb, Academic Press, 2021, vol. 102, pp. 1–80.

19 R. Quiñones, R. J. Iuliucci, G. Behnke, R. Brown, D. Shoup, T. M. Riedel, C. Plavchak, B. E. Lininger and J. M. Spehar, *J. Pharm. Biomed. Anal.*, 2018, **148**, 163–169.

20 E. Chaloupecká, V. Tyrpekl, K. Bártová, Y. Nishiyama and M. Dračínský, *Solid State Nucl. Magn. Reson.*, 2024, **130**, 101921.

21 Z. Rehman, J. Lubay, W. T. Franks, A. P. Bartók, E. K. Corlett, B. Nguyen, G. Scrivens, B. M. Samas, H. Frericks-Schmidt and S. P. Brown, *Faraday Discuss.*, 2025, **255**, 222–243.

22 Y. Dai, V. Terskikh, A. Brinmkmann and G. Wu, *Cryst. Growth Des.*, 2020, **20**, 7484–7491.

23 J. Herzfeld and A. E. Berger, *J. Chem. Phys.*, 1980, **73**, 6021–6030.

24 R. K. Harris, *J. Pharm. Pharmacol.*, 2007, **59**, 225–239.

25 P. E. Hansen, *Molecules*, 2024, **29**, 336.

26 B. I. Dunlap and N. Rosch, in *Adv. Quantum Chem.*, ed. P.-O. Löwdin, Academic Press, 1990, vol. 21, pp. 317–339.

27 M. Dračínský, in *Modern NMR Crystallography: Concepts and Applications*, ed. D. L. Bryce, Royal Society of Chemistry, 2025, vol. 36.

28 A. L. Reviglio, F. A. Martínez, M. D. A. Montero, Y. Garro-Linck, G. A. Aucar, N. R. Sperandeo and G. A. Monti, *RSC Adv.*, 2021, **11**, 7644–7652.

29 E. K. Corlett, H. Blade, L. P. Hughes, P. J. Sidebottom, D. Walker, R. I. Walton and S. P. Brown, *CrystEngComm*, 2019, **21**, 3502–3516.

30 J. R. Yates, S. E. Dobbins, C. J. Pickard, F. Mauri, P. Y. Ghi and R. K. Harris, *Phys. Chem. Chem. Phys.*, 2005, **7**, 1402–1407.

31 C. Poidevin, G. L. Stoychev, C. Riplinger and A. A. Auer, *J. Chem. Theory Comput.*, 2022, **18**, 2408–2417.

32 C. J. Pickard and F. Mauri, *Phys. Rev. B:Condens. Matter Mater. Phys.*, 2001, **63**, 245101.

33 C. Bonhomme, C. Gervais, F. Babonneau, C. Coelho, F. Pourpoint, T. Azaïs, S. E. Ashbrook, J. M. Griffin, J. R. Yates, F. Mauri and C. J. Pickard, *Chem. Rev.*, 2012, **112**, 5733–5779.

34 S. E. Ashbrook and D. McKay, *Chem. Commun.*, 2016, **52**, 7186–7204.

35 T. Charpentier, *Solid State Nucl. Magn. Reson.*, 2011, **40**, 1–20.

36 M. Kellner, J. B. Holmes, R. Rodriguez-Madrid, F. Viscosi, Y. Zhang, L. Emsley and M. Ceriotti, *J. Phys. Chem. Lett.*, 2025, **16**, 8714–8722.

37 F. M. Paruzzo, A. Hofstetter, F. Musil, S. De, M. Ceriotti and L. Emsley, *Nat. Commun.*, 2018, **9**, 4501.

38 E. Chaloupecká, O. Socha and M. Dračínský, *Solid State Nucl. Magn. Reson.*, 2025, **138**, 102019.

39 C. Quaranta, I. d'Anciães Almeida Silva, S. Moos, E. Bartalucci, L. Hendrickx, B. M. D. Fahl, C. Pasqualini, F. Puccetti, M. Zobel, C. Bolm and T. Wiegand, *Angew. Chem., Int. Ed.*, 2024, **63**, e202410801.

40 A.-A. Lafrance, M. Girard and D. L. Bryce, *Solid State Nucl. Magn. Reson.*, 2024, 101925.

41 L. Hendrickx, C. Quaranta, E. Fuchs, M. Plekhanov, M. Zobel, C. Bolm and T. Wiegand, *Molecules*, 2025, **30**, 3745.

42 T. Kameda and H. Teramoto, *Magn. Reson. Chem.*, 2006, **44**, 318–324.

43 M. Dračínský, J. Vícha, K. Bártová and P. Hodgkinson, *ChemPhysChem*, 2020, **21**, 2075–2083.

44 J. P. Perdew, K. Burke and M. Ernzerhof, *Phys. Rev. Lett.*, 1996, **77**, 3865–3868.

45 J. P. Perdew, K. Burke and M. Ernzerhof, *Phys. Rev. Lett.*, 1997, **78**, 1396.

46 M. Dračínský, P. Unzueta and G. J. O. Beran, *Phys. Chem. Chem. Phys.*, 2019, **21**, 14992–15000.

47 S. A. Ramos, L. J. Mueller and G. J. O. Beran, *Faraday Discuss.*, 2025, **255**, 119–142.

48 S. G. J. van Meerten, W. M. J. Franssen and A. P. M. Kentgens, *J. Magn. Reson.*, 2019, **301**, 56–66.

49 B. H. Toby and R. B. Von Dreele, *J. Appl. Crystallogr.*, 2013, **46**, 544–549.

50 G. Kresse and J. Furthmüller, *Phys. Rev. B:Condens. Matter Mater. Phys.*, 1996, **54**, 11169–11186.

51 G. Kresse and J. Furthmüller, *Comput. Mater. Sci.*, 1996, **6**, 15–50.

52 G. Kresse and D. Joubert, *Phys. Rev. B:Condens. Matter Mater. Phys.*, 1999, **59**, 1758–1775.

53 G. Kresse and J. Hafner, *Phys. Rev. B:Condens. Matter Mater. Phys.*, 1993, **47**, 558–561.

54 W. S. Morgan, J. E. Christensen, P. K. Hamilton, J. J. Jorgensen, B. J. Campbell, G. L. W. Hart and R. W. Forcade, *Comput. Mater. Sci.*, 2020, **173**, 109340.

55 J. Tao, J. P. Perdew, V. N. Staroverov and G. E. Scuseria, *Phys. Rev. Lett.*, 2003, **91**, 146401.

56 A. V. Krukau, O. A. Vydrov, A. F. Izmaylov and G. E. Scuseria, *J. Chem. Phys.*, 2006, **125**, 224106.

57 P. J. Stephens, F. J. Devlin, C. F. Chabalowski and M. J. Frisch, *J. Phys. Chem.*, 1994, **98**, 11623–11627.

58 S. Grimme, J. Antony, S. Ehrlich and H. Krieg, *J. Chem. Phys.*, 2010, **132**, 154104.

59 J. R. Yates, C. J. Pickard and F. Mauri, *Phys. Rev. B:Condens. Matter Mater. Phys.*, 2007, **76**, 024401.
60 G. A. de Wijs, R. Laskowski, P. Blaha, R. W. A. Havenith, G. Kresse and M. Marsman, *J. Chem. Phys.*, 2017, **146**, 064115.
61 P. E. Blöchl, *Phys. Rev. B:Condens. Matter Mater. Phys.*, 1994, **50**, 17953–17979.
62 E. V. Boldyreva, E. N. Kolesnik, T. N. Drebushchak, H. Ahsbahs, J. A. Beukes and H.-P. Weber, *Z. Kristallogr. – Cryst. Mater.*, 2005, **220**, 58–65.
63 M. N. Frey, M. S. Lehmann, T. F. Koetzle and W. C. Hamilton, *Acta Crystallogr., Sect. B:Struct. Sci.*, 1973, **29**, 876–884.
64 M. Hong, *J. Am. Chem. Soc.*, 2000, **122**, 3762–3770.
65 Z. Wu, N. Tjandra and A. Bax, *J. Am. Chem. Soc.*, 2001, **123**, 3617–3618.
66 A. Venkatesh, D. Gioffrè, B. A. Atterberry, L. Rochlitz, S. L. Carnahan, Z. Wang, G. Menzildjian, A. Lesage, C. Copéret and A. J. Rossini, *J. Am. Chem. Soc.*, 2022, **144**, 13511–13525.
67 J. Koppe, A. V. Yakimov, D. Gioffre, M. E. Usteri, T. Vosegaard, G. Pintacuda, A. Lesage, A. J. Pell, S. Mitchell, J. Perez-Ramirez and C. Coperet, *Nature*, 2025, **642**, 613–619.
68 Z. J. Berkson, W. Cao, D. Gioffrè, C. J. Kaul, L. Lätsch, Y. Kakiuchi, A. Yakimov and C. Copéret, *JACS Au*, 2025, **5**, 2911–2931.
69 F. Blanc, J.-M. Basset, C. Copéret, A. Sinha, Z. J. Tonzetich, R. R. Schrock, X. Solans-Monfort, E. Clot, O. Eisenstein, A. Lesage and L. Emsley, *J. Am. Chem. Soc.*, 2008, **130**, 5886–5900.
70 M. M. Maricq and J. S. Waugh, *J. Chem. Phys.*, 1979, **70**, 3300–3316.
71 W. T. Dixon, *J. Chem. Phys.*, 1982, **77**, 1800–1809.
72 Z. Gan, *J. Am. Chem. Soc.*, 1992, **114**, 8307–8309.
73 O. N. Antzutkin, S. C. Shekar and M. H. Levitt, *J. Magn. Reson., Ser. A*, 1995, **115**, 7–19.
74 S. L. Gann, J. H. Baltisberger and A. Pines, *Chem. Phys. Lett.*, 1993, **210**, 405–410.
75 F. Allen, *Acta Crystallogr., Sect. B:Struct. Sci.*, 2002, **58**, 380–388.
76 Ł. Szeleszczuk, D. M. Pisklak and M. Zielińska-Pisklak, *J. Comput. Chem.*, 2018, **39**, 853–861.
77 R. K. Harris, P. Hodgkinson, C. J. Pickard, J. R. Yates and V. Zorin, *Magn. Reson. Chem.*, 2007, **45**, S174–S186.
78 D. H. Brouwer, K. P. Langendoen and Q. Ferrant, *Can. J. Chem.*, 2011, **89**, 737–744.